ACS APPLIED MATERIALS & INTERFACES

www.acsami.org

Research Article

Two-Dimensional Magnetic Semiconducting Heterostructures of Single-Layer CrI_3–CrI_2

Peigen Li,[‖] Nanshu Liu,[‖] Jihai Zhang,[‖] Shenwei Chen, Xuhan Zhou, Donghui Guo, Cong Wang, Wei Ji,* and Dingyong Zhong*

Cite This: *ACS Appl. Mater. Interfaces* 2023, 15, 19574–19581

Read Online

ACCESS | Metrics & More | Article Recommendations | Supporting Information

ABSTRACT: Single-layer heterostructures of magnetic materials are unique platforms for studying spin-related phenomena in two dimensions (2D) and have promising applications in spintronics and magnonics. Here, we report the fabrication of 2D magnetic lateral heterostructures consisting of single-layer chromium triiodide (CrI_3) and chromium diiodide (CrI_2). By carefully adjusting the abundance of iodine based on molecular beam epitaxy, single-layer CrI_3–CrI_2 heterostructures were grown on Au(111) surfaces with nearly atomic-level seamless boundaries. Two distinct types of interfaces, i.e., zigzag and armchair interfaces, have been identified by means of scanning tunneling microscopy. Our scanning tunneling spectroscopy study combined with density functional theory calculations indicates the existence of spin-polarized ground states below and above the Fermi energy localized at the boundary. Both the armchair and zigzag interfaces exhibit semiconducting nanowire behaviors with different spatial distributions of density of states. Our work presents a novel low-dimensional magnetic system for studying spin-related physics with reduced dimensions and designing advanced spintronic devices.

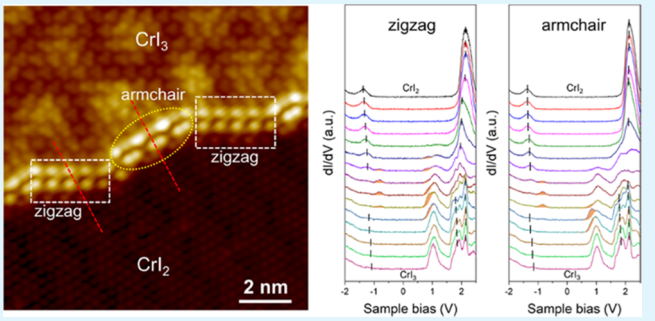

KEYWORDS: *two-dimensional magnetism, chromium iodide, lateral heterostructures, interfacial states, scanning tunneling microscopy*

INTRODUCTION

Two-dimensional (2D) van der Waals (vdW) heterostructures, which are formed by integrating different 2D vdW materials together, give rise to abundant and unique structures and have potential applications in electronics and optoelectronics.[1,2] Considering the 2D nature of these layered materials, the vdW heterostructures can be divided into vertical ones or lateral ones. 2D vertical heterostructures can be obtained by mechanical exfoliation and layer-by-layer stacking of vdW materials.[3] Owing to the weak vdW interactions between the layers, there is no requirement of lattice matching at the interfaces and therefore it is much flexible for the choice of materials constructing the heterostructures. In 2D vertical heterostructures, however, intercalating contamination[4,5] and stacking orientational randomness[5] should be eliminated in order to improve the performance and repeatability of devices. On the other hand, 2D lateral heterostructures are constructed by intralayer chemical bonding between different 2D materials.[6] The relatively robust bonding makes the junctions more stable. More importantly, since the single-layer feature is maintained in 2D lateral heterostructures, they are suitable for studying quantum phenomena in reduced dimensions and for fabricating ultrathin electronic and spintronic devices.[7] So far, high-quality 2D lateral heterostructures of transition-metal chalcogenides have been fabricated by multistep chemical vapor deposition (CVD) methods.[8] Desired heterostructure arrays can also be achieved by combining CVD with laser or electronic etching processes.[9,10] Other 2D lateral heterostructures grown by molecular beam epitaxy (MBE), such as hBN/graphene,[11] germanene/stanene,[12] and $SnSe_2$/SnSe,[13] have also been reported. Although the preparation processes for 2D materials are relatively mature, growing in-plane 2D vdW heterojunctions with seamless interfacial connection is challenging due to the restriction of lattice matching between the component materials.

Recently, monolayer (ML) CrI_3[14] and bilayer (BL) $Cr_2Ge_2Te_6$[15] have been proved to exist in spontaneous ferromagnetism, opening the door to explore 2D magnetism in layered vdW materials. By introducing magnetic order into 2D heterostructures, unique physical phenomena may occur, such as topological quantum states,[16−18] topological superconductivity,[19,20] and polarized valley states.[21,22] Magnetic tunneling junctions, based on vdW vertical heterostructures

Received: December 14, 2022
Accepted: March 28, 2023
Published: April 4, 2023

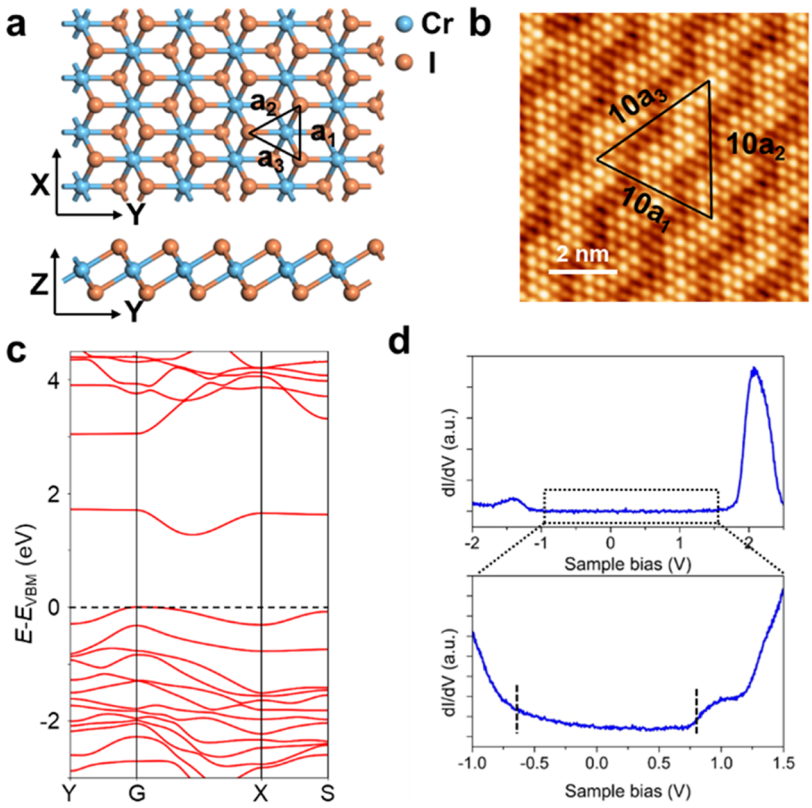

Figure 1. Atomic and electronic structures of single-layer CrI_2. (a) Atomic structure of single-layer CrI_2. (b) Typical high-resolution STM image of CrI_2 grown on Au(111) (0.8 V, 100 pA). (c) Calculated band structure of freestanding ML CrI_2 with an effective U value of 3 eV for Cr. The valence band maximum (VBM) is set to zero. (d) dI/dV spectrum of single-layer CrI_2 on Au(111) (2 V, 100 pA for upper and −1 V, 200 pA for lower panels, respectively). The vertical dashed lines in the lower panel are VBM and conduction band minimum (CBM).

consisting of four CrI_3 layers and two graphene layers, can achieve a 19 000% change in magnetoresistance.[23] So far, various vertical heterostructures based on 2D magnetic materials have been fabricated.[24−28] However, 2D magnetic lateral heterostructures are still rarely reported. One case is the lateral heterostructures of magnetic metallic $CrTe_2$ and semiconducting $CrTe_3$, which have been experimentally realized recently.[29,30] The lateral heterostructure composed of ferromagnetic (FM) WS_2 and nonmagnetic MoS_2 is theoretically predicted to be used as spin-valley beam filters/splitters.[31] In addition, such lateral junctions provide promising platforms to study one-dimensional (1D) physics and can serve as 1D spin channels for spintronic devices.[32,33] Considering these potential applications in spintronics, seeking in-plane heterostructures between 2D magnetic semiconductors is a topic of concern.

Here, we report on the growth of high-quality lateral heterostructures of two types of single-layer vdW magnetic semiconductors CrI_3 and CrI_2 by MBE. Atomically resolved scanning tunneling microscopy (STM) was performed to reveal the atomic structures of the heterojunctions. We found that single-layer CrI_3 and CrI_2, which have honeycomb and triangular lattices, respectively, can form nearly atomic-level seamless junctions. Two types of interfacial motifs, i.e., zigzag and armchair, were identified. Scanning tunneling spectroscopy (STS) and density functional theory (DFT) calculations were conducted to study the electronic structures of the CrI_3−CrI_2 lateral heterostructure. Spin-polarized ground states were revealed at the interface of the heterostructures, which exhibit 1D semiconducting characteristics.

RESULTS AND DISCUSSION

As shown in Figure 1a, the fully relaxed lattice of single-layer CrI_2 is a three-atomic-layer structure with one close-packed layer of Cr sandwiched by two layers of I atoms. Figure 1b shows the atomic-resolved STM image of the ML CrI_2 on the Au(111) surface. The three nearest-neighboring iodine atoms in the topmost layer form an isosceles triangle with experimentally measured lattice constants of a_1 = 4.0 Å and a_2 = a_3 = 4.2 Å, consistent with the values from our DFT calculations (a_1 = 3.96 Å and a_2 = a_3 = 4.23 Å) and earlier STM measurements reported elsewhere.[34−36] A moiré pattern between CrI_2 and the underlying iodine buffer layer on the Au(111) surface leads to the "zigzag" superstructure in Figure 1b, which is similar to single-layer CrI_3 on Au(111).[34]

DFT calculations were carried out to obtain the electronic structures of ML CrI_2 considering the spin−orbit coupling (SOC) effect. We first optimized the lattice constants and atomic positions using a structure with a C_3 rotational symmetry taking a FM order. The relaxed structure spontaneously breaks the C_3 symmetry with an enlarged Cr−I bond length along the Y axis, indicating a Jahn−Teller (J−T) effect of ML CrI_2. The magnetic ground state of ML CrI_2 is a stripped ABAB antiferromagnetic (AFM) order under Coulomb energy (U) values ranging from 0.0 to 6.0 eV (Figure S1). The linear response method deriving U = 4.9 eV gives the upper limit of U value. The ABAB-AFM order can also be obtained by the HSE06 functional considering the exact exchange interaction. In addition, the band gap increases from 0.33 to 1.90 eV with U values growing from 0 to 5.8 eV (see Figure S2). The band gap of ML CrI_2 is 1.27 eV (Figure

https://doi.org/10.1021/acsami.2c22494
ACS Appl. Mater. Interfaces 2023, 15, 19574−19581

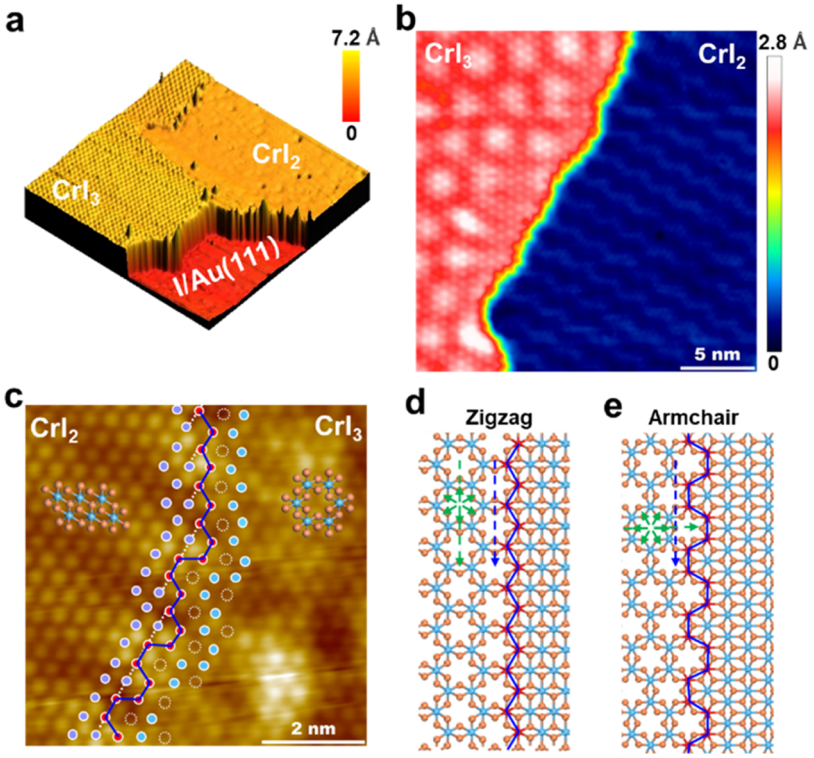

Figure 2. Single-layer CrI_3−CrI_2 lateral heterostructures on Au(111). (a) Large-scale STM image (2.0 V, 100 pA, 125 × 125 nm^2). (b) Zoomed STM image (1.5 V, 80 pA). (c) Atomic-resolved STM image near the interface (0.3 V, 100 pA). Dark and light blue circles represent Cr atoms from CrI_2 to CrI_3, while red circles represent Cr atoms at the interface. The white dotted circles represent the hexagonal honeycomb center of CrI_3. (d, e) Structural models of CrI_3−CrI_2 lateral heterostructures with zigzag and armchair boundaries.

1c) with an effective U of 3 eV, which is commonly used in Cr-based systems.[37,38] Both the valence and conduction bands are comprised of the Cr e_g orbitals and the I−p_x/p_y orbitals (Figure S3), similar to those of ML CrI_3.[31] Considering the octahedron crystal field, the five 3d orbitals of the Cr atom are degenerated into three t_{2g} (d_{xy}, d_{yz}, and d_{xz}) and two e_g ($d_{x^2-y^2}$ and d_{z^2}) orbitals, which further split into a d_{z^2} orbital with lower energy and a higher $d_{x^2-y^2}$ one due to the J−T effect (Figure S3). Three d electrons of each Cr atom in CrI_2 will fill the t_{2g} orbitals, while another electron occupies the d_{z^2} orbital, corresponding to a high spin state with a local magnetic moment of 3.92 μ_B on each Cr atom.

Our STS result (upper of Figure 1d) with a setpoint of 2.0 V, 100 pA indicates the onsets of unoccupied and occupied states at 1.8 and −1.2 eV, respectively, corresponding to a gap of about 3 eV, similar to the case with graphitized SiC as the substrate.[34,36] However, our calculations by the DFT+U method indicate a much smaller band gap of 1.27 eV. To unveil possible implicit states close to the Fermi energy, we conducted further STS measurements with the tip closer to the sample (setpoint −1 V, 200 pA), as shown in the lower panel of Figure 1d. In this case, an additional bulge near 0.8 eV emerges on the unoccupied side, which is assigned to the conduction band edge of CrI_2. To determine the valence band edge of CrI_2, we compared the STS results of CrI_2 and iodine layer on Au(111), as shown in Figure S4. We found that the local density of states (LDOS) of CrI_2 increases significantly from −0.6 eV, while the LDOS of the iodine layer exhibits a flat feature from −0.35 to −1.0 eV (blue dashed line in Figure S4). As a result, we obtain a reduced band gap of 1.4 eV, closer to the calculated value. The inferior visibility of the STS signal from the states near 0.8 eV may be explained by their localized feature at the Cr atoms, which is underneath the surface I layer (see the orbital-resolved band structures in Figure S3). Another possible explanation is that the differential conductivity is relatively insensitive to the states far from Γ point in k-space.[39]

Single-layer CrI_3−CrI_2 lateral heterostructures are fabricated by adjusting the I flux during the MBE growth or by prolonged annealing of as-grown single-layer CrI_3 under ultrahigh vacuum (UHV) environment (see the Methods section). Heating to a proper temperature can gradually release iodine from certain iodine-based compounds, such as CuI,[40−42] CrI_3,[34,36] which provides a suitable pathway to synthesize CrI_3−CrI_2 lateral heterostructures. Figure S5 exhibits the annealing-induced phase transition from CrI_3 to CrI_2, which reveals that prolonged annealing at 150 °C is a suitable method for the preparation of CrI_3−CrI_2 lateral heterostructures. Figure 2a shows the large-scale topography of a single-layer CrI_3−CrI_2 lateral heterostructure on the Au(111) surface. The CrI_3 and CrI_2 regions are separated by a well-defined boundary with distinct morphological differences. In the zoom-in image (Figure 2b), single-layer CrI_3 exhibits a dotted moiré superstructure and has a hexagonal lattice composed of I atom trimers with lattice constant a = 6.95 Å. In contrast, single-layer CrI_2 shows a zigzag moiré superstructure and has a distorted close-packed hexagonal lattice composed of upper-layer I atoms. In the atomic-resolved STM image of CrI_3−CrI_2 lateral heterostructures (Figure 2c), we can observe an atomic-level seamless interface between the CrI_3 and CrI_2 regions. The formation of atomically sharp boundaries is beneficial from the small lattice mismatch between the two materials. In Figure 2c, the arrangement of the atoms at the boundary is labeled, indicating the almost identical I sublattices and different Cr

https://doi.org/10.1021/acsami.2c22494
ACS Appl. Mater. Interfaces 2023, 15, 19574−19581

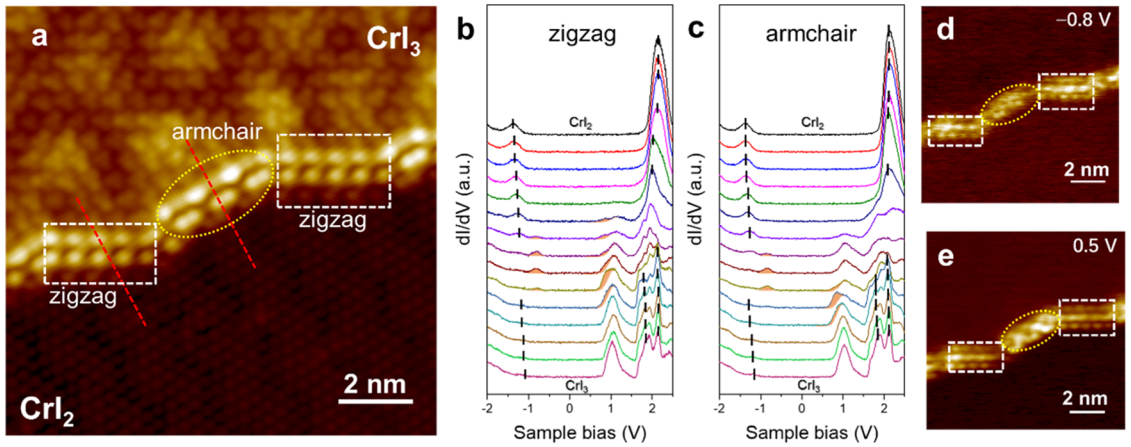

Figure 3. STS at the CrI_2−CrI_3 interfaces. (a) Typical STM image of the heterostructure consisting of zigzag and armchair boundaries (0.6 V, 100 pA). (b, c) Typical STS results across the zigzag and armchair boundaries (red lines in panel (a)). The short black lines show the energy shift of the peaks. The boundary states are filled with orange color. (d, e) STS mappings for both boundaries at a bias of −0.8 and 0.5 V, 100 pA, respectively.

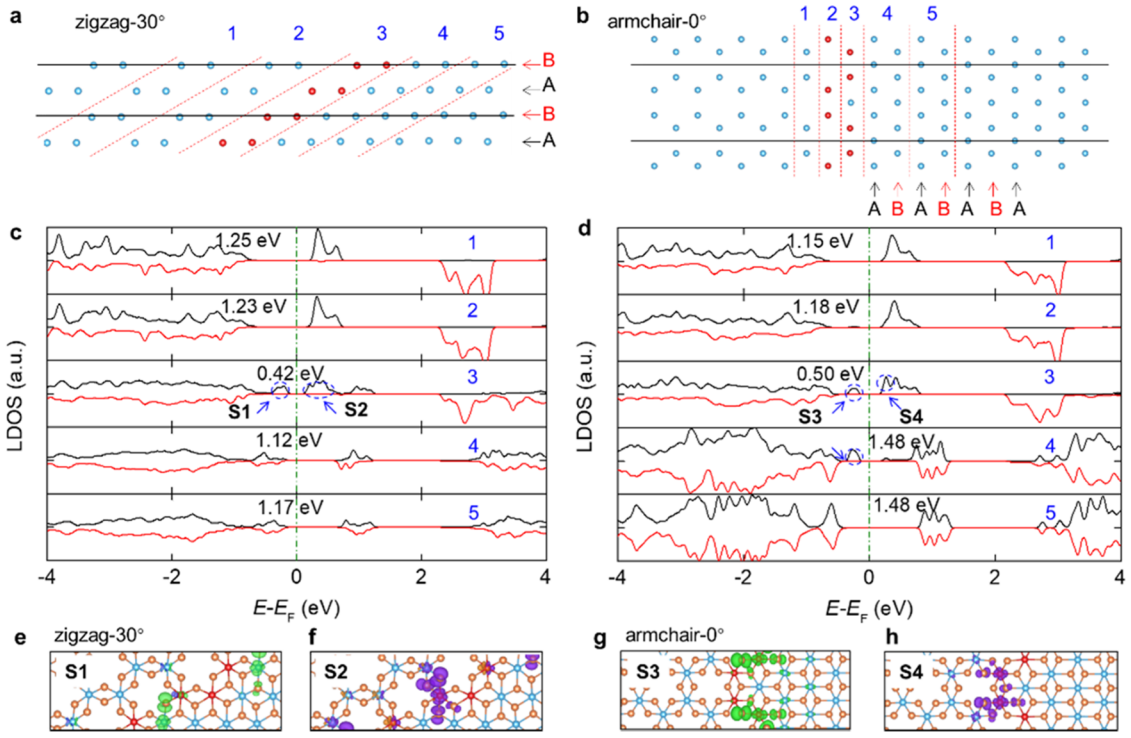

Figure 4. Atomic and electronic structures of CrI_3−CrI_2 lateral heterostructures by DFT calculations. (a, b) Atomic structures of zigzag-30° and armchair-0° boundaries. The atoms of CrI_2 and CrI_3 in different regions are marked by red lines and blue numbers. The ABAB-AFM stripes of CrI_2 are labeled. Blue and red circles are interfacial and bulk Cr atoms, respectively. Iodine atoms are hidden. Black lines are lattices of supercells. (c, d) LDOS at different regions as labeled in panels (a) and (b). The numbers are the band gaps in the spin-up channel. (e−h) Spatial distributions of the boundary states noted by S1−S4 in panels (c, d). The isosurface value is set to 1.2×10^{-3} e/Bohr^3.

sublattices, i.e., honeycomb lattice in CrI_3 while triangular lattice in CrI_2 (light and dark blue circles). There are two types of atomic arrangements at the interface: the top part of Figure 2c displays a zigzag orientation, while the bottom part of Figure 2c displays an armchair orientation. The structural models of the zigzag and armchair boundaries are shown in Figure 2d,e.

Figure 3a shows a typical high-resolution STM image of the CrI_3−CrI_2 lateral heterostructure with a sample bias of 0.6 V, exhibiting brighter contrast at the interface of the junction. Furthermore, the zigzag and armchair boundaries display different contrast patterns. The zigzag boundary shows a $\sqrt{3}$ I−I period, similar to its atomic structure, while the armchair boundary shows an extra 3 times period of I−I distance, owing to the different chemical surroundings of I atoms at the boundary. The 3 times period at the armchair boundary can also be seen in the STS mapping of the heterostructure (Figure S6). A series of STS measurements across the boundaries (STS profile) were performed to further reveal the local density of states (LDOS) of the CrI_3−CrI_2 lateral heterostructures. Typical STS profiles of the zigzag and armchair boundaries are shown in Figure 3b,c. From both types of boundaries, extra states localized at the interfaces were observed at about ±0.8 V (filled with orange color in Figure 3b,c; see also in Figure S7).

https://doi.org/10.1021/acsami.2c22494
ACS Appl. Mater. Interfaces 2023, 15, 19574−19581

Besides, these boundary states, the occupied and unoccupied bands for both the CrI_3 and CrI_2 sides show a mixing behavior at the interfaces. From both sides to the boundary, bulk states show band bending and weakening characteristics. In detail, the upward (downward) bending of the occupied band on the CrI_2 (CrI_3) side was observed, resulting in their convergence at the boundary. On the other hand, a downward bending exists for both the unoccupied bands of CrI_3 and CrI_2. The band bending may originate from the charge transfer due to different valence states of Cr atoms (+2 for CrI_2 and +3 for CrI_3), lattice mismatch,[43] charge transfer between bulk states and the boundary states,[44] or combined effects from the strain and charge transfer.[45]

The identical features in the STS results for both boundaries are discussed above. We then turn to their differences. A significant difference of the electronic states at the boundaries for the zigzag and armchair boundaries is in the shift behavior of unoccupied bands of CrI_2 before it hybrids with that of CrI_3. In the case of the zigzag boundary, the peak at about 2 eV in CrI_2 smoothly moves to 1.7 eV and converges with the unoccupied bands of CrI_3. Such movements are not significant in the case of the armchair boundary, which shows a broadened behavior at the boundary. The other difference is the position of boundary states in energy space. The occupied states at the zigzag interface are slightly closer to the Fermi energy than those at the armchair ones, while the unoccupied states show opposite features. Such results can be seen clearer in the STS profile across the boundary with a smaller tip−sample distance in Figure S7. In STS mapping results shown in Figure 3d,e, the zigzag boundary (marked by a white box) is brighter than the armchair one (marked by yellow ellipses) with a bias of −0.8 V, while the contrast inverses with a bias of 0.5 V, well consistent with our STS profile results.

Figure 4a,b shows the relaxed structural models of lateral heterostructures along the zigzag and armchair directions in DFT calculations. For zigzag interfaces, two types of interfaces were observed in our experiment, one with the ABAB-AFM stripe rotated by 30° relative to the boundary (zigzag-30° shown in Figure 3a) and the other one with a stripe perpendicular to the boundary (zigzag-90° in Figure S8). In the case of armchair boundaries, we only observed the ABAB stripe along the interface (armchair-0°; Figure 3a), while armchair-60° was not observed, probably due to the higher interfacial energy induced by larger lattice mismatch than the other interface types. The simulated STM images based on the models are consistent with our experiments (Figure S9). Figure 4c,d shows the LDOS of the interfacial and domain regions (labeled in Figure 4a,b), both of which show semiconducting properties, similar to a recent theoretical work.[46] In the domain regions away from the zigzag-30° (armchair-0°) boundary, the calculated band gaps of CrI_3 and CrI_2 are 1.25 eV (1.15 eV) and 1.17 eV (1.48 eV), respectively, which are well close to those of pristine ones (1.17 eV for CrI_3 and 1.27 eV for CrI_2), indicating that the supercells used in our DFT calculations are large enough to avoid possible interactions between mirror images. The band gaps are significantly smaller than those in domain regions for both boundaries, consistent with the observed STS results (Figure 3b,c). Partial charge densities of boundary states (labeled as S1−S4 in Figure 4c,d) at the zigzag-30° and armchair-0° boundaries (Figure 4e−h) are localized at the boundaries. Furthermore, the ground states of the four interfacial states are spin-polarized and localized around the different Cr columns (Figure 4e−h), implying that the electronic and spin transport across or along the interface may hold exotic low-dimensional electronic or spintronic phenomena.[47] From the calculated density of states, one can find that the energy differences between the local boundary states S1 of zigzag-30° and S3 of armchair-0° relative to the VBM of CrI_3 are 0.69 and 0.56 eV, respectively. This indicates that the occupied states of the zigzag-30° interface are closer to the Fermi energy, consistent with the experimental STS mapping results. However, the energy differences between S2 and S4 relative to the CBM of CrI_3 are 0.14 and 0.09 eV, which are much smaller than those of S1 and S3 to VBM. The boundary states S2 and S4 thus show a strong hybridization with the conduction band of CrI_3 for the two interfaces, which can also be seen in the experimental section STS results (Figure 3b,c).

A rotation of the ABAB-AFM stripe of CrI_2 induces a significant lattice distortion and thus results in local strain at the interface, which may increase the interfacial energy. It is expected that the ABAB stripes exhibit a specific direction relative to the interface. For zigzag-90°, spin-polarized boundary states are predicted from our DFT calculation (Figure S10). Compared with zigzag-30°, one significant difference is that the polarization of the boundary state at CBM changes from spin-up to spin-down channel. On the other hand, the lattice of armchair-60° is strongly distorted, as shown in Figure S10b, which has a significant effect on the electronic structure on the CrI_2 side with spin exchange splitting (Figure S10d). The band gap of CrI_2 in the bulk region enlarges to 11% compared with the strain-free ML.

The growth process inevitably introduces defects at the interfaces, especially iodine defects/vacancies, which may significantly affect the performance of the CrI_3−CrI_2 heterostructure.[48,49] As shown in Figure S11, iodine vacancies at the interface can change the spatial distribution of the boundary states and even quench the boundary states. Further calculations were carried out to reveal the effect of iodine vacancies on the electronic properties of CrI_2−CrI_3 heterojunctions. Two types of I vacancies were considered, including a three- (V_{I3}) and a two-coordinated (V_{I2}) one at the zigzag interfaces (see Figure S12). A spin-polarized boundary state is only induced in the spin-up component near the Fermi level by V_{I3}, though the defect-free interface possesses spin-polarized boundary states in both spin channels (the up panel in Figure S12d). Unlike V_{I3}, the boundary states are absent for both spin channels for V_{I2}, as plotted in the bottom panel of Figure S12d. These changes vary the band gap by up to 0.16 eV in these two defective interfaces.

CONCLUSIONS

In conclusion, we successfully prepared single-layer CrI_3−CrI_2 lateral heterostructures on Au(111) surfaces by MBE. Zigzag and armchair boundaries were identified at the atomic-level seamless interfaces by high-resolution STM. There are extra occupied and unoccupied boundary states localized at the interfaces, exhibiting characteristics of 1D semiconducting nanowires and having spin-polarized ground states.

The 2D lateral heterostructures between two magnetic semiconductors with atomic-level seamless interfaces are promising platforms for future studies on low-dimensional magnetoelectric phenomena. Given the FM and AFM orders on both sides, single-layer CrI_3−CrI_2 heterostructures as semiconducting junctions can be utilized for constructing novel in-plane spintronic devices. Furthermore, the boundaries

https://doi.org/10.1021/acsami.2c22494
ACS Appl. Mater. Interfaces 2023, 15, 19574−19581

of the heterostructures resemble 1D wires of spin-polarized semiconductors, where electrons and holes from both sides converge on the boundaries, making the interfaces suitable platforms for research on 1D physics.[33] Compared with the boundary states observed in ML−BL WSe_2 or $MoSe_2$ systems,[50] the boundary states at the CrI_3−CrI_2 heterostructures with spin-polarized ground states may hold unprecedented spin-related phenomena. In particular, since the 2D honeycomb CrI_3 lattice possesses topological magnons,[51,52] the CrI_3−CrI_2 lateral heterostructure is a possible system to realize topological magnon edge states carrying dissipationless spin current.

METHODS

Experimental Details. STM experiments at 78 K were conducted on a low-temperature STM system designed by Kehui Wu, Institute of Physics, Chinese Academy of Sciences, while STM experiments at 5 K and STS experiments were carried out on a Unisoku 1300 ULT-VMF system. Single-layer CrI_3−CrI_2 lateral heterostructures were fabricated on Au(111) (Mateck GmbH) substrates under UHV condition with a base pressure of 8×10^{-10} mbar. Au(111) surfaces were repeatedly cleaned by 1.5 kV Ar^+ ions sputtering for 15 min and annealing at 450−500 °C for 10 min. Iodine source was obtained by thermal decomposition of a CrI_3 powder (purity 90%) at 220 °C under UHV. Chromium powder (purity 99.996%, Alfa Aesar) was evaporated from a Knudsen cell at 980 °C under UHV. Single-layer CrI_3 films were grown on Au(111) maintained at 150 °C via codeposition of chromium and iodine with a flux of ∼1:20. Single-layer CrI_3−CrI_2 lateral heterostructures were prepared by codeposition with reduced iodine flux or by vacuum annealing of single-layer CrI_3 films at 150 °C for 1 h, which results in the partial decomposition of single-layer CrI_3 and the formation of CrI_2. All STM experiments were performed with constant current mode using an electrochemically etched tungsten tip. The tunneling spectra were obtained by a lock-in technique with a sinusoidal modulation signal of an amplitude of 10 mV at a frequency of 987 Hz.

Calculation Details. Density functional theory (DFT) calculations were performed using the generalized gradient approximation (GGA) for the exchange−correlation potential with a plane-wave basis and the projected-augmented wave (PAW) method as implanted in the Vienna *ab initio* Simulation Package (VASP). The energy cutoff for the plane wave was set to 700 eV for structural relaxation and 600 eV for electronic structural calculations. The optB86b-vdW exchange functional was adapted to obtain comparable lattice parameters of freestanding ML CrI_2 with the experimental data. An effective Hubbard on-site Coulomb parameter U = 3.0 eV was used for Cr atoms to account for the strong correlation effect. The supercells of CrI_2/CrI_3 lateral heterostructures with armchair and zigzag directions have in-plane dimensions of a = 79.91 Å, b = 12.13 Å and a = 76.26 Å, b = 7.00 Å and a vacuum region of 20 Å in the out-of-plane direction, respectively. The first Brillouin zones of the supercells were sampled by the Monkhorst−Pack k-point meshes with 1 × 4 × 1 for armchair and 1 × 6 × 1 for zigzag heterostructures. With fixed supercells of heterostructures, all of the model structures were fully relaxed for the ionic and electronic degrees of freedom with convergence criteria of 10^{-5} eV for energy and 0.01 eV/Å for force.

ASSOCIATED CONTENT

Supporting Information

The Supporting Information is available free of charge at https://pubs.acs.org/doi/10.1021/acsami.2c22494.

Calculated magnetic ground state of monolayer CrI_2; band structures of freestanding CrI_2 monolayer with different effective U values; band structures of freestanding CrI_2 monolayer for different orbitals of Cr and I;dI/dV spectra of single-layer CrI_2 and iodine layer on Au(111); annealing-induced phase transition from CrI_3 to CrI_2; STS along the boundaries; STS across the boundaries with different tip−sample distances; the CrI_3−CrI_2 lateral heterostructure with zigzag-90° and armchair-60° interfaces; STM simulation results of the armchair and zigzag heterostructures; and effect of I vacancies for CrI_3−CrI_2 heterostructures (PDF)

AUTHOR INFORMATION

Corresponding Authors

Wei Ji − *Beijing Key Laboratory of Optoelectronic Functional Materials & Micro-Nano Devices, Department of Physics, Renmin University of China, 100872 Beijing, China;* orcid.org/0000-0001-5249-6624; Email: wji@ruc.edu.cn

Dingyong Zhong − *School of Physics, Sun Yat-sen University, 510275 Guangzhou, China; State Key Laboratory of Optoelectronic Materials and Technologies, Sun Yat-sen University, 510275 Guangzhou, China*; Email: dyzhong@mail.sysu.edu.cn

Authors

Peigen Li − *School of Physics, Sun Yat-sen University, 510275 Guangzhou, China; State Key Laboratory of Optoelectronic Materials and Technologies, Sun Yat-sen University, 510275 Guangzhou, China*

Nanshu Liu − *Beijing Key Laboratory of Optoelectronic Functional Materials & Micro-Nano Devices, Department of Physics, Renmin University of China, 100872 Beijing, China*

Jihai Zhang − *School of Physics, Sun Yat-sen University, 510275 Guangzhou, China; State Key Laboratory of Optoelectronic Materials and Technologies, Sun Yat-sen University, 510275 Guangzhou, China;* orcid.org/0000-0002-7695-4869

Shenwei Chen − *School of Physics, Sun Yat-sen University, 510275 Guangzhou, China; State Key Laboratory of Optoelectronic Materials and Technologies, Sun Yat-sen University, 510275 Guangzhou, China;* orcid.org/0000-0003-4669-5015

Xuhan Zhou − *School of Physics, Sun Yat-sen University, 510275 Guangzhou, China; State Key Laboratory of Optoelectronic Materials and Technologies, Sun Yat-sen University, 510275 Guangzhou, China;* orcid.org/0000-0002-5019-9092

Donghui Guo − *School of Physics, Sun Yat-sen University, 510275 Guangzhou, China*

Cong Wang − *Beijing Key Laboratory of Optoelectronic Functional Materials & Micro-Nano Devices, Department of Physics, Renmin University of China, 100872 Beijing, China*

Complete contact information is available at: https://pubs.acs.org/10.1021/acsami.2c22494

Author Contributions

‖P.L., N.L., and J.Z. contributed equally to this work.

Notes

The authors declare no competing financial interest.

ACKNOWLEDGMENTS

The authors gratefully acknowledge the National Natural Science Foundation of China (Grant Nos. 11974431, 92165204, 11832019, 11974422, and 12204534). D.Z. thanks the financial support from the Guangdong Major Project of

Basic and Applied Basic Research (2021B0301030002). W.J. gratefully acknowledges financial support from the Ministry of Science and Technology (MOST) of China (Grant No. 2018YFE0202700), the Strategic Priority Research Program of Chinese Academy of Sciences (Grant No. XDB30000000), the Fundamental Research Funds for the Central Universities, and the Research Funds of Renmin University of China [Grant No. 22XNKJ30]. N.L. was supported by the China Postdoctoral Science Foundation (2022M713447). Calculations were performed at the Physics Lab of High-Performance Computing of the Renmin University of China and Shanghai Supercomputer Center.

REFERENCES

(1) Liu, Y.; Zhang, S.; He, J.; Wang, Z. M.; Liu, Z. Recent Progress in the Fabrication, Properties, and Devices of Heterostructures Based on 2D Materials. *Nano-Micro Lett.* **2019**, *11*, 1−13.

(2) Zhou, X.; Hu, X.; Yu, J.; Liu, S.; Shu, Z.; Zhang, Q.; Li, H.; Ma, Y.; Xu, H.; Zhai, T. 2D Layered Material-Based van der Waals Heterostructures for Optoelectronics. *Adv. Funct. Mater.* **2018**, *28*, No. 1706587.

(3) Novoselov, K. S.; Mishchenko, A.; Carvalho, A.; Castro Neto, A. H. 2D Materials and van der Waals Heterostructures. *Science* **2016**, *353*, No. aac9439.

(4) Haigh, S. J.; Gholinia, A.; Jalil, R.; Romani, S.; Britnell, L.; Elias, D. C.; Novoselov, K. S.; Ponomarenko, L. A.; Geim, A. K.; Gorbachev, R. Cross-Sectional Imaging of Individual Layers and Buried Interfaces of Graphene-Based Heterostructures and Superlattices. *Nat. Mater.* **2012**, *11*, 764−767.

(5) Yang, W.; Chen, G.; Shi, Z.; Liu, C.-C.; Zhang, L.; Xie, G.; Cheng, M.; Wang, D.; Yang, R.; Shi, D.; Watanabe, K.; Taniguchi, T.; Yao, Y.; Zhang, Y.; Zhang, G. Epitaxial Growth of Single-Domain Graphene on Hexagonal Boron Nitride. *Nat. Mater.* **2013**, *12*, 792−797.

(6) Wang, J.; Li, Z.; Chen, H.; Deng, G.; Niu, X. Recent Advances in 2D Lateral Heterostructures. *Nano-Micro Lett.* **2019**, *11*, No. 48.

(7) Hus, S. M.; Li, A.-P. Spatially-Resolved Studies on the Role of Defects and Boundaries in Electronic Behavior of 2D Materials. *Prog. Surf. Sci.* **2017**, *92*, 176−201.

(8) Zhang, Z.; Chen, P.; Duan, X.; Zang, K.; Luo, J.; Duan, X. Robust Epitaxial Growth of Two-Dimensional Heterostructures, Multiheterostructures, and Superlattices. *Science* **2017**, *357*, 788−792.

(9) Mahjouri-Samani, M.; Lin, M. W.; Wang, K.; Lupini, A. R.; Lee, J.; Basile, L.; Boulesbaa, A.; Rouleau, C. M.; Puretzky, A. A.; Ivanov, I. N.; Xiao, K.; Yoon, M.; Geohegan, D. B. Patterned Arrays of Lateral Heterojunctions within Monolayer Two-Dimensional Semiconductors. *Nat. Commun.* **2015**, *6*, No. 7749.

(10) Afaneh, T.; Sahoo, P. K.; Nobrega, I. A. P.; Xin, Y.; Gutiérrez, H. R. Laser-Assisted Chemical Modification of Monolayer Transition Metal Dichalcogenides. *Adv. Funct. Mater.* **2018**, *28*, No. 1802949.

(11) Liu, L.; Park, J.; Siegel, D. A.; McCarty, K. F.; Clark, K. W.; Deng, W.; Basile, L.; Idrobo, J. C.; Li, A.-P.; Gu, G. Heteroepitaxial Growth of Two-Dimensional Hexagonal Boron Nitride Templated by Graphene Edges. *Science* **2014**, *343*, 163−167.

(12) Ogikubo, T.; Shimazu, H.; Fujii, Y.; Ito, K.; Ohta, A.; Araidai, M.; Kurosawa, M.; Le Lay, G.; Yuhara, J. Continuous Growth of Germanene and Stanene Lateral Heterostructures. *Adv. Mater. Interfaces* **2020**, *7*, No. 1902132.

(13) Tian, Z.; Zhao, M.; Xue, X.; Xia, W.; Guo, C.; Guo, Y.; Feng, Y.; Xue, J. Lateral Heterostructures Formed by Thermally Converting n-Type $SnSe_2$ to p-Type SnSe. *ACS Appl. Mater. Interfaces* **2018**, *10*, 12831−12838.

(14) Huang, B.; Clark, G.; Navarro-Moratalla, E.; Klein, D. R.; Cheng, R.; Seyler, K. L.; Zhong, D.; Schmidgall, E.; McGuire, M. A.; Cobden, D. H.; Yao, W.; Xiao, D.; Jarillo-Herrero, P.; Xu, X. Layer-Dependent Ferromagnetism in a van der Waals Crystal down to the Monolayer Limit. *Nature* **2017**, *546*, 270−273.

(15) Gong, C.; Li, L.; Li, Z.; Ji, H.; Stern, A.; Xia, Y.; Cao, T.; Bao, W.; Wang, C.; Wang, Y.; Qiu, Z. Q.; Cava, R. J.; Louie, S. G.; Xia, J.; Zhang, X. Discovery of Intrinsic Ferromagnetism in Two-Dimensional van der Waals Crystals. *Nature* **2017**, *546*, 265−269.

(16) Pan, J.; Yu, J.; Zhang, Y.-F.; Du, S.; Janotti, A.; Liu, C.-X.; Yan, Q. Quantum Anomalous Hall Effect in Two-Dimensional Magnetic Insulator Heterojunctions. *npj Comput. Mater.* **2020**, *6*, No. 152.

(17) Zhang, H.; Qin, W.; Chen, M.; Cui, P.; Zhang, Z.; Xu, X. Converting a Two-Dimensional Ferromagnetic Insulator into a High-Temperature Quantum Anomalous Hall System by means of an Appropriate Surface Modification. *Phys. Rev. B* **2019**, *99*, No. 165410.

(18) Hou, Y.; Kim, J.; Wu, R. Magnetizing Topological Surface States of Bi_2Se_3 with a CrI_3 Monolayer. *Sci. Adv.* **2019**, *5*, No. eaaw1874.

(19) Kezilebieke, S.; Huda, M. N.; Vaňo, V.; Aapro, M.; Ganguli, S. C.; Silveira, O. J.; Głodzik, S.; Foster, A. S.; Ojanen, T.; Liljeroth, P. Topological Superconductivity in a van der Waals Heterostructure. *Nature* **2020**, *588*, 424−428.

(20) Kezilebieke, S.; Huda, M. N.; Dreher, P.; Manninen, I.; Zhou, Y.; Sainio, J.; Mansell, R.; Ugeda, M. M.; van Dijken, S.; Komsa, H.-P.; Liljeroth, P. Electronic and Magnetic Characterization of Epitaxial VSe_2 Monolayers on Superconducting $NbSe_2$. *Commun. Phys.* **2020**, *3*, 116.

(21) Zhang, H.; Yang, W.; Ning, Y.; Xu, X. Abundant Valley-Polarized States in Two-Dimensional Ferromagnetic van der Waals Heterostructures. *Phys. Rev. B* **2020**, *101*, No. 205404.

(22) Shayan, K.; Liu, N.; Cupo, A.; Ma, Y.; Luo, Y.; Meunier, V.; Strauf, S. Magnetic Proximity Coupling of Quantum Emitters in WSe_2 to van der Waals Ferromagnets. *Nano Lett.* **2019**, *19*, 7301−7308.

(23) Song, T.; Cai, X.; Tu, M. W.-Y.; Zhang, X.; Huang, B.; Wilson, N. P.; Seyler, K. L.; Zhu, L.; Taniguchi, T.; Watanabe, K.; McGuire, M. A.; Cobden, D. H.; Xiao, D.; Yao, W.; Xu, X. Giant Tunneling Magnetoresistance in Spin-Filter van der Waals Heterostructures. *Science* **2018**, *360*, 1214−1218.

(24) Zhong, D.; Seyler, K. L.; Linpeng, X.; Cheng, R.; Sivadas, N.; Huang, B.; Schmidgall, E.; Taniguchi, T.; Watanabe, K.; McGuire, M. A.; Yao, W.; Xiao, D.; Fu, K.-M. C.; Xu, X. Van der Waals Engineering of Ferromagnetic Semiconductor Heterostructures for Spin and Valleytronics. *Sci. Adv.* **2017**, *3*, No. e1603113.

(25) Jiang, S.; Xie, H.; Shan, J.; Mak, K. F. Exchange Magnetostriction in Two-Dimensional Antiferromagnets. *Nat. Mater.* **2020**, *19*, 1295−1299.

(26) Chen, X.; Wang, H.; Liu, H.; Wang, C.; Wei, G.; Fang, C.; Wang, H.; Geng, C.; Liu, S.; Li, P.; Yu, H.; Zhao, W.; Miao, J.; Li, Y.; Wang, L.; Nie, T.; Zhao, J.; Wu, X. Generation and Control of Terahertz Spin Currents in Topology-Induced 2D Ferromagnetic Fe_3GeTe_2/Bi_2Te_3 Heterostructures. *Adv. Mater.* **2022**, *34*, No. 2270067.

(27) Cai, X.; Song, T.; Wilson, N. P.; Clark, G.; He, M.; Zhang, X.; Taniguchi, T.; Watanabe, K.; Yao, W.; Xiao, D.; McGuire, M. A.; Cobden, D. H.; Xu, X. Atomically Thin $CrCl_3$: An In-Plane Layered Antiferromagnetic Insulator. *Nano Lett.* **2019**, *19*, 3993−3998.

(28) Zhang, L.; Huang, X.; Dai, H.; Wang, M.; Cheng, H.; Tong, L.; Li, Z.; Han, X.; Wang, X.; Ye, L.; Han, J. Proximity-Coupling-Induced Significant Enhancement of Coercive Field and Curie Temperature in 2D van der Waals Heterostructures. *Adv. Mater.* **2020**, *32*, No. 2002032.

(29) Li, R.; Nie, J.-H.; Xian, J.-J.; Zhou, J.-W.; Lu, Y.; Miao, M.-P.; Zhang, W.-H.; Fu, Y.-S. Planar Heterojunction of Ultrathin $CrTe_3$ and $CrTe_2$ van der Waals Magnet. *ACS Nano* **2022**, *16*, 4348−4356.

(30) Yao, J.; Wang, H.; Yuan, B.; Hu, Z.; Wu, C.; Zhao, A. Ultrathin Van der Waals Antiferromagnet $CrTe_3$ for Fabrication of In-Plane $CrTe_3/CrTe_2$ Monolayer Magnetic Heterostructures. *Adv. Mater.* **2022**, *34*, No. 2200236.

(31) Ghadiri, H.; Saffarzadeh, A. Band-Offset-Induced Lateral Shift of Valley Electrons in Ferromagnetic MoS_2/WS_2 Planar Heterojunctions. *J. Appl. Phys.* **2018**, *123*, No. 104301.

https://doi.org/10.1021/acsami.2c22494
ACS Appl. Mater. Interfaces 2023, 15, 19574−19581

(32) Mishra, V.; Salahuddin, S. One-Dimensional Spin Channel in Two-Dimensional Transition Metal Dichalcogenide Heterostructures. *IEEE Trans. Nanotechnol.* **2018**, *17*, 1053−1057.
(33) Ávalos-Ovando, O.; Mastrogiuseppe, D.; Ulloa, S. E. Lateral Heterostructures and One-Dimensional Interfaces in 2D Transition Metal Dichalcogenides. *J. Phys.: Condens. Matter* **2019**, *31*, No. 213001.
(34) Peng, L.; Zhao, J.; Cai, M.; Hua, G.-Y.; Liu, Z.-Y.; Xia, H.-N.; Yuan, Y.; Zhang, W.-H.; Xu, G.; Zhao, L.-X.; Zhu, Z.-W.; Xiang, T.; Fu, Y.-S. Mott Phase in a van der Waals Transition-Metal Halide at Single-Layer Limit. *Phys. Rev. Res.* **2020**, *2*, No. 023264.
(35) Li, P.; Wang, C.; Zhang, J.; Chen, S.; Guo, D.; Ji, W.; Zhong, D. Single-Layer CrI_3 Grown by Molecular Beam Epitaxy. *Sci. Bull.* **2020**, *65*, 1064−1071.
(36) Cai, X.; Xu, Z.; Ji, S.H.; Li, N.; Chen, X. Molecular Beam Epitaxy Growth of Iodide Thin Films. *Chin. Phys. B* **2021**, *30*, No. 028102.
(37) Liu, N.; Zhou, S.; Zhao, J. High-Curie-Temperature Ferromagnetism in Bilayer CrI_3 on Bulk Semiconducting Substrates. *Phys. Rev. Mater.* **2020**, *4*, No. 094003.
(38) Liu, N.; Zhou, S.; Zhao, J. Photoinduced Spin Injection and Ferromagnetism in 2D Group III Monochalcogenides. *J. Phys. Chem. Lett.* **2022**, *13*, 590−597.
(39) Zhang, C.; Chen, Y.; Johnson, A.; Li, M.-Y.; Li, L.-J.; Mende, P. C.; Feenstra, R. M.; Shih, C.-K. Probing Critical Point Energies of Transition Metal Dichalcogenides: Surprising Indirect Gap of Single Layer WSe_2. *Nano Lett.* **2015**, *15*, 6494−6500.
(40) Yamada, N.; Ino, R.; Ninomiya, Y. Truly Transparent p-Type γ-CuI Thin Films with High Hole Mobility. *Chem. Mater.* **2016**, *28*, 4971−4981.
(41) Yang, C.; Souchay, D.; Kneiß, M.; Bogner, M.; Wei, H. M.; Lorenz, M.; Oeckler, O.; Benstetter, G.; Fu, Y. Q.; Grundmann, M. Transparent Flexible Thermoelectric Material Based on Non-Toxic Earth-Abundant p-Type Copper Iodide Thin Film. *Nat. Commun.* **2017**, *8*, No. 16076.
(42) Mulla, R.; Rabinal, M. K. Defect-Controlled Copper Iodide: A Promising and Ecofriendly Thermoelectric Material. *Energy Technol.* **2018**, *6*, 1178−1185.
(43) Huang, Y. L.; Chen, Y.; Zhang, W.; Quek, S. Y.; Chen, C. H.; Li, L. J.; Hsu, W. T.; Chang, W. H.; Zheng, Y. J.; Chen, W.; Wee, A. T. Bandgap Tunability at Single-Layer Molybdenum Disulphide Grain Boundaries. *Nat. Commun.* **2015**, *6*, No. 6298.
(44) Ly, T. H.; Perello, D. J.; Zhao, J.; Deng, Q.; Kim, H.; Han, G. H.; Chae, S. H.; Jeong, H. Y.; Lee, Y. H. Misorientation-Angle-Dependent Electrical Transport across Molybdenum Disulfide Grain Boundaries. *Nat. Commun.* **2016**, *7*, No. 10426.
(45) Wang, D.; Yu, H.; Tao, L.; Xiao, W.; Fan, P.; Zhang, T.; Liao, M.; Guo, W.; Shi, D.; Du, S.; Zhang, G.; Gao, H. Bandgap Broadening at Grain Boundaries in Single-Layer MoS_2. *Nano Res.* **2018**, *11*, 6102−6109.
(46) Zhao, Y.; Liu, H.; Zhao, J.; Gao, J. In-Plane CrI_2/CrI_3 2D Superlattices: Novel Electronic Properties and Strain Induced Phase Transition. *Phys. Chem. Chem. Phys.* **2022**, *24*, 25530−25536.
(47) Huang, C.; Wu, S.; Sanchez, A. M.; Peters, J. J.; Beanland, R.; Ross, J. S.; Rivera, P.; Yao, W.; Cobden, D. H.; Xu, X. Lateral Heterojunctions within Monolayer $MoSe_2$-WSe_2 Semiconductors. *Nat. Mater.* **2014**, *13*, 1096−1101.
(48) Cao, Z.; Harb, M.; Lardhi, S.; Cavallo, L. Impact of Interfacial Defects on the Properties of Monolayer Transition Metal Dichalcogenide Lateral Heterojunctions. *J. Phys. Chem. Lett.* **2017**, *8*, 1664−1669.
(49) Zhao, J.; Cheng, K.; Han, N.; Zhang, J. Growth Control, Interface Behavior, Band Alignment, and Potential Device Applications of 2D Lateral Heterostructures. *Wiley Interdiscip. Rev.: Comput. Mol. Sci.* **2018**, *8*, No. e1353.
(50) Zhang, C.; Chen, Y.; Huang, J.-K.; Wu, X.; Li, L.-J.; Yao, W.; Tersoff, J.; Shih, C.-K. Visualizing Band Offsets and Edge States in Bilayer−Monolayer Transition Metal Dichalcogenides Lateral Heterojunction. *Nat. Commun.* **2016**, *7*, No. 10349.
(51) Owerre, S. A. A First Theoretical Realization of Honeycomb Topological Magnon Insulator. *J. Phys.: Condens. Matter* **2016**, *28*, No. 386001.
(52) Pershoguba, S. S.; Banerjee, S.; Lashley, J. C.; Park, J.; Ågr en, H.; Aeppli, G.; Balatsky, A. V. Dirac Magnons in Honeycomb Ferromagnets. *Phys. Rev. X* **2018**, *8*, No. 011010.